Dual T_1/T_2 Nanoscale Coordination Polymers as Novel Contrast Agents for MRI: a Preclinical Study for Brain Tumor

S. Suárez-García,[†] *N. Arias-Ramos,*[§,‡] *C. Frias,*[†] *A. Paula Candiota,*[‡, §,$] *C. Arús,*[§,‡,$] *J. Lorenzo,*[§,$,]* *D. Ruiz-Molina,*[†] *F. Novio*[†,#,]**

† Catalan Institute of Nanoscience and Nanotechnology (ICN2), CSIC and BIST, Campus UAB, Bellaterra, 08193 Barcelona, Spain.

§ Departament de Bioquímica i Biologia Molecular, Universitat Autònoma de Barcelona, 08193 Cerdanyola del Vallès, Spain.

‡ Centro de Investigación Biomédica en Red: Bioingeniería, Biomateriales y Nanomedicina, 08193 Cerdanyola del Vallès, Spain.

$ Institut de Biotecnologia i de Biomedicina. Departament de Bioquimica i Biologia Molecular. Universitat Autònoma de Barcelona, 08193 Cerdanyola del Vallès, Barcelona, Spain.

Departament de Química, Universitat Autònoma de Barcelona, 08193 Cerdanyola del Vallès, Barcelona, Spain.

* Dr Julia Lorenzo. Ph: +(34) 935868936 Fax: +(34) 935812011. E-mail: julia.lorenzo@uab.cat

** Dr Fernando Novio. Ph: +(34) 937373630 Fax: +(34) 937372648. E-mail: fernando.novio@icn2.cat

KEYWORDS

Nanoparticles, Coordination Polymers, Contrast agents, Dual imaging, MRI, Nanomedicine.

ABSTRACT

In the last years, extensive attention has been paid on designing and developing functional imaging contrast agents for providing accurate non-invasive evaluation of pathology *in vivo*. However, the issue of false-positives or ambiguous imaging and the lack of a robust strategy for simultaneous dual-mode imaging remain to be fully addressed. One effective strategy for improving it is to rationally design magnetic resonance imaging (MRI) contrast agents (CAs) with intrinsic T_1/T_2 dual-mode imaging features. In this work, the development and characterization of one-pot synthesized nanostructured coordination polymers (NCPs) which exhibit dual mode T_1/T_2 MRI contrast behaviour is described. The resulting material comprises the combination of different paramagnetic ions (Fe^{3+}, Gd^{3+}, Mn^{2+}) with selected organic ligands able to induce the polymerization process and nanostructure stabilization. Among them, the Fe-based NCPs showed the best features in terms of colloidal stability, low toxicity, and dual T_1/T_2 MRI contrast performance overcoming the main drawbacks of reported CAs. The dual-mode CA capability was evaluated by different means: *in vitro* phantoms, *ex vivo* and *in vivo* MRI, using a preclinical model of murine glioblastoma. Surprisingly, the *in vivo* MRI shows its T_1 and T_2 high contrast potential, allowing simultaneous recording of positive and negative contrast images in a very short period of time while being safer for the body. Moreover, the biodistribution assays reveals the persistence of the nanoparticles in the tumor and subsequent gradual clearance denoting their biodegradability. After a comparative study with commercial CAs, the results suggest these nanoplatforms as promising candidates for the development of dual-mode MRI CAs with clear advantages.

1. Introduction

Magnetic resonance imaging (MRI) is a powerful technique for gathering tomographic images of biological soft tissues in a non-invasive manner with a high spatial resolution and depth penetration. This radiation-free technique enables the coding of nuclear magnetization into 2D/3D images, being the most used tool in clinical diagnosis. The signal intensity of proton-based MRI (^{1}H-MRI) depends on a combination of factors: proton density, longitudinal (T_1) and transversal (T_2) relaxivity times and the cell microenvironment.[1,2] However, the intrinsic contrast provided by the combination of these factors and the biological changes due to a disease are not enough for obtaining accurate and sensitive diagnosis. For these reasons, the use of contrast agents (CAs) in MRI diagnosis is needed in order to improve image resolution due to their selective accumulation in the Region-Of-Interest (ROI). CAs can shorten longitudinal and transverse relaxation of protons respectively causing a positive enhancement (i.e. brighter image) in T_1-weighted (T_{1w}) MRI and negative enhancement (i.e. darker image) in T_2-weighted (T_{2w}) MRI in comparison with pre-contrast images.[3,4,5] Unfortunately, most of the T_1 and T_2 CAs clinically approved for MRI diagnosis, have associated several disadvantages. Usually, T_1 CAs are based on chelating complexes of paramagnetic gadolinium.[6] The presence of Gd^{3+} has been related with some technical issues and health risks such as headache, nausea, dizziness and severe nephrogenic system fibrosis (NSF).[7,8,9,10,11] Furthermore, long-term deposition of Gd in the human brain due to their incomplete clearance from the organism, has been recently reported.[12,13] Apart from Gd, manganese (II) has been presented as alternative CA for T_{1w} images. However, the accumulative toxicity arising from Mn^{2+} which induces neurological degeneration or oxidative stress in cells, might limit its clinical application. On the other hand, typical contrast agents in T_{2W} images are generally based on superparamagnetic iron oxide nanoparticles or ferrites (e.g. SPIONs).[14,15] Nevertheless, the analysis process of resulting T_{2w} images are laborious due to the low signal body regions that can be confused with hemorrhages, calcifications, fat, blood clots and other possible artefacts in damaged tissue.[16] Although most of the recent developments are based on inorganic nanoparticles,[17] in the last years hybrid metal-organic[18] and metal-free organic[19] nanoparticles has been proposed as good CAs for MRI due to their minimal cytotoxicity and biodegradability in comparison to metal-based contrast agents.

At this point, and in spite of extensive research has been carried out to obtain novel MRI CAs, the single mode contrast agents are far from being optimum. Current CAs exhibit major limitations in terms of MRI artefacts, imaging ambiguities and health risks. In order to overcome these limitations, a great effort has been done in the combination of techniques in order to stablish dual-imaging procedures (e.g. PET/MRI). Nevertheless, due the confounding results and the difficult of clinical implementation of the dual-imaging techniques, only a few of them have earned admittance to clinical applications. For this reason, dual-modal MRI has demonstrated enough merits and good perspectives in practical diagnosis to avoid such limitations by simply adjusting the acquisition sequences.[20] Furthermore, T_1/T_2 dual-mode MRI is performed by single scanner, ensuring a perfect match of spatial and temporal imaging parameters being more beneficial compared to other bimodal imaging techniques.[21,22]

In this scenario, the development of novel T_1/T_2 dual-mode contrast agents (DMCAs) with clinical proof of their *in vivo* performance is a pressing concern. DMCAs can be selectively tuned to visualize by bright or dark T_{1w} and T_{2w} images in order to obtain complementary and more precise information by cross-validation of the possible false-positives.[23] The synthesis of T_1/T_2 DMCAs in a single platform is currently a challenge. In this sense, different strategies based on nanoscale engineering have been developed during the last years. These strategies consisted mainly in i) direct conjugation of T_1 compounds (e.g., Gd or Mn-containing systems) and T_2 compounds (e.g., SPIONs).[21,24-26] (ii) T_2 materials doped with T_1 contrast materials;[19,27-29] (iii) magnetic nanoparticles with rational modulation of size and magnetization;[3,30] and (iv) integration of T_1 contrast materials with nonmagnetic porous materials.[31-34] However, these strategies are often involved in laborious procedures with multi-step synthesis. Furthermore, the possibility of quenching effect between T_1 and T_2 due to the interaction between both relaxation times requires a delicate control limiting their production and clinical applications.[23]

Based on this rationale, nanoscale coordination polymers (NCPs) have appeared during the last years as good candidates for their use in medical applications. The interest of NCPs lies in their rational chemical design based on multiple combinations between metal ions and polydentate ligands. The potential multifunctionality of these nanosystems implies longer blood circulation times as compared to common chelates, less metal leaching and greater area between magnetically centers and the tissue due to the increased surface-to-volume ratio. Encouragingly, previous studies showed that biodegradable NCPs could provide T_{1w} properties and be combined with T_{2w} contrast agents to obtain nanosystems with dual-mode MRI properties.[35] Different approaches have been reported recently in order to synthesize DMCAs by Eu co-doping of a Gd NCP complex,[36] the use of porphyrin ligands for the chelation of Fe,[37] or polydopamine-based coordination complex and its affinity for Fe ions.[33]

Despite the progress of DMCAs, some questions remain need to be addressed before the clinical application of DMCAs become a reality: i) facile synthesis procedures with possibilities for scale up, ii) chemically stable in biological environment by non- toxicity and non-accumulation in the organism (avoiding the use of Gd and Mn ions) and iii) high efficiency in different tissues by good biodistribution (low uptake in liver and kidneys).[38] These key parameters have to be considered during the rational design of novel DMCAs overcoming the main drawbacks of current clinical approved CAs.

Therefore, there is still need to overcome the disadvantages of single modality CAs by the preparation of robust DMCAs which are supposed to minimize the risks of ambiguity and improve the diagnostic sensitivity. Herein we demonstrate the intrinsic ability of NCPs complexes based on paramagnetic ions (Fe^{3+}, Gd^{3+}, Mn^{2+}) to generate in a facile, robust and reproducible one-pot synthesis biodegradable DMCAs nanoparticles. In a deeper study, we selected the Fe-based NCPs (Fe-NCP) nanosystem as a suitable candidate for preclinical studies, which overcomes the main issues of contrast agents: i) cheap one-pot procedure, ii) chemically stable, iii) non-toxic and biocompatible, iv) intrinsically T_1 and T_2 imaging capabilities *in vitro* and *in vivo* and v) good biodistribution with low uptake by liver and kidneys. This rational design provides a protocol for the synthesis of novel systems in successful way, which reduces the main limitations of other reported systems. To the best of our knowledge, this is the first report on the fabrication of Fe-NCP for T_{1w}/T_{2w} contrast enhancement for the diagnosis and visualization of glioblastoma *in vivo* allowing the imaging of cerebral lesions. Our work would help to the development of novel one-pot NCP-based DMCA systems as a valid strategy with potential applications in theranostic and clinical translation to T_1/T_2 dual-mode MRI.

2. Experimental section

2.1 Materials. Solvents and starting materials were purchased from Sigma–Aldrich (Merck, Madrid, Spain) and used as received, without further purification, unless otherwise stated. 1,4-Bis(imidazol-1-ylmethyl)benzene (L1, Bix) was synthesized according to previously reported methodology.[39]

2.2 Characterization. Scanning electron microscopy (SEM) was performed for platinum-metallized samples on a FEI Quanta 650 FEG (Thermo Fisher Scientific, Eindhoven, The Netherlands) in mode operation of secondary electrons (SE) with a beam voltage between 5 and 20 kV. Fourier-transform infrared spectra (FT-IR) were recorded on a Tensor 27 FT-IR spectrometer (Bruker Optik GmbH, Berlin, Germany) with KBr pellets. Ultraviolet-visible spectroscopy (UV-Vis) was performed using a Cary 4000 UV-vis spectrometer (Agilent Technologies, Santa Clara, CA, USA) within range wavelengths from 200 to 800 nm and a 1 cm path length quartz cuvette (QS 10 mm). The baseline was corrected using a blank sample of pure solvent. All the measurements were taken under atmosphere conditions. Dynamic light scattering (DLS) measurements for obtaining size distribution and zeta potential (ζ-potential) of the nanostructures were performed using a Zetasizer Nano ZS 3600 (Malvern Instruments, U.K.). All analyzed samples were diluted in order to obtain a concentration of nanoparticles suitable for the experimental calculation of size dispersion. The data reported are values coming from the mean of measurements for each sample which were measured per quadruplicate. Inductive coupled plasma-mass spectroscopy measurements (ICP-MS) were obtained using an ICP-MS NexION 300X (Perkin Elmer, San Francisco, CA, USA). All samples were measured in argon atmosphere. X-ray photoelectron spectroscopy (XPS) measurements were performed with a Phoibos 150 analyzer (SPECS GmbH, Berlin, Germany) in ultra-high vacuum conditions (based pressure 10^{-10} mbar). Monochromatic Al Kα was used as X-ray source (1486.6 eV). The electron energy analyzer was operated with pass energy of 50 eV. The analyzer was located perpendicular to the sample surface. The data was collected every eV with a dwell time of 0.5 s and treated with CasaXPS version 2.317PR1.1 /Casa Software LTD, Teignmouth, UK).

2.3 Synthesis of Fe-NCP, Gd-NCP and Mn-NCP. 1,4-Bis(imidazole-1-ylmethil)-benzene (L1, Bix – 60 mg, 0.25 mmol) and 3,4-dihydroxycinnamic acid (L2, dhc – 90 mg, 0.5 mmol) were dissolved in 15 mL of ethanol under vigorous and homogenous magnetic stirring (700 rpm) during 30 minutes at room temperature. Subsequently, the solution was treated with an aqueous solution containing metal salt either $Fe(CH_3COO)_2$ (43.5 mg, 0.25 mmol in 2 mL H_2O; for Fe-NCP), $Gd(CH_3COO)_3 \cdot 6H_2O$ (83 mg, 0.25 mmol in 2 mL H_2O; for Gd-NCP) or $Mn(CH_3COO)_2$ (61 mg, 0.25 mmol in 2 mL H_2O; for Mn-NCP), which turned the solution either black-purple, yellow and dark green, respectively, and led to rapid formation of a precipitate.

Fe-NCP: IR (KBr): 3140 (w, δ (C–H_{ring})), 2974 (w), 1678 (w), 1623 (s, ν(C=N)), 1575 (w), 1519 (s, ν(C–H_{ring})), 1481 (s, ν(C–O)), 1398 (s), 1263 (s, ν(C–O)), 1105 (m), 980 (m), 864 (s, δ(N-H_{ring})), 521 (s, Fe–O) cm^{-1}. Anal. Calcd (%) for Fe-NCP: C 47.03, H 4.58, N 5.86; found: C 47.00, H 3.82, N 5.92. ICP-MS Calcd (%) for Fe-NCP: Fe 12.05; found: Fe 11.85. Compositional formula: $Fe_1L1_{0.49}L2_{1.30}(AcO^-)_{0.25}(H_2O)_{3.82}$.

Gd-NCP: IR (KBr): 2926 (w, δ (C–H_{ring})), 2853 (w, ν(C–$H_{aliphatic}$)), 1631 (s, ν(C=N)), 1520 (w, νC–H_{ring})), 1416 (s, ν(C–O)), 1271 (s, ν(C–O)), 1121 (m), 978 (m), 864 (s, δ(N–H_{ring})), 542 (s, Gd–O) cm^{-1}. Anal. Calcd (%) for Gd-NCP: C 38.79, H 4.06, N 5.89; found: C 38.00, H 3.20, N 6.08. ICP-MS Calcd (%) for Gd-NCP: Gd 29.50; found: Gd 29.90. Compositional formula: $Gd_1L1_{0.57}L2_{1.03}(AcO^-)_{0.30}(H_2O)_{3.11}$.

Mn-NCP: IR (KBr): 3128 (w, δ (C–H_{ring})), 2972 (w), 2934 (w, ν(C–$H_{aliphatic}$)), 1629 (s, ν(C=N)), 1520 (w, νC–H_{ring})), 1489 (s, ν(C–O)), 1261 (s, ν(C–O)), 1110 (m), 859 (s, δ(N–H_{ring}), 558 (s, Mn–O) cm^{-1}. Anal. Calcd (%) for Mn-NCP: C 53.07, H 5.19, N 8.44; found: C 52.40, H

4.10, N 8.26. ICP-MS Calcd (%) for Mn-NCP: Mn 7.74; found: Mn 7.67. Compositional formula: $Mn_1L1_{1.07}L2_{1.82}(AcO^-)_{0.28}(H_2O)_{3.09}$.

2.4 Synthesis of GdDTPA-NCP. 1,4-Bis(imidazole-1-ylmethil)-benzene (L1, Bix – 60 mg, 0.25 mmol) and diethylenetriaminepentaacetic acid (L3, DTPA – 84 mg, 0.25 mmol) were dissolved in 15 mL of ethanol under vigorous and homogenous magnetic stirring (700 rpm). Subsequently, the solution was treated with and aqueous solution containing metal salt $Gd(CH_3COO)_3 \cdot 6H_2O$ (Gadolinium (III) acetate - 83 mg, 0.25 mmol in 2 mL H_2O), which turned the solution deep yellow and led to rapid formation of a precipitate.

GdDTPA-NCP: IR (KBr): 2980 (w, δ (C–H_{ring})), 1678 (w, ν(C=N)), 1598 (w, νC–H_{ring})), 1411 (s, ν(C–O)), 1266 (s, ν(C–O)), 1118 (m), 931 (m), 866 (s, δ(N–H_{ring}), 549 (s, Gd–O) cm^{-1}. Anal. Calcd (%) for GdDTPA-NCP: C 46.75, H 4.87, N 13.92; found: C 46.89, H 4.70, N 14.45. ICP-MS Calcd (%) for GdDTPA-NCP: Gd 20.07; found: Gd 20.50. Compositional formula: $Gd_1L1_{1.39}L3_{0.70}(H_2O)_{1.2}$.

All the synthesis reactions were carried out during 30 minutes under room temperature and at atmospheric conditions. The obtained precipitates were centrifuged (7500 rpm, 5 min) and washed with water and ethanol. The precipitates were vacuum dried and the solvent was removed.

2.5 Functionalization of NCPs with BSA. All the systems synthesized were functionalized with Bovine or Mouse Serum Albumin (BSA or MSA, respectively) in order to obtain better dispersions reducing the formation of aggregates in solution. All the solutions were prepared in a phosphate buffer (PBS, pH = 7.4) with a physiological concentration of BSA (0.5 mM). The nanoparticles were added to the solution containing BSA and PBS under magnetic stirring at 37 °C during 1h.

2.6 *In vitro* assays

2.6.1. Quantitative magnetic resonance imaging phantoms (MRI-Phantoms). The samples of nanoparticles were dispersed using agarose (1%) in phosphate buffer solution (PBS) at pH = 7.4. For all families of nanostructures, five samples at decreasing concentrations (0.6, 0.3, 0.1, 0.05 and 0 mM of metal mL^{-1}) were prepared in 1.5 mL Eppendorf tubes. The total volume was adjusted up to 1 mL with agarose in PBS. The dispersions were well dispersed in an ultrasound bath just before the solidification of medium. Acquisition sequences for assessing longitudinal relaxation (T_1) and transversal relaxation (T_1) were carried out with 7T (300 MHz) Bruker BioSpec 70/30 USR spectrometer (Bruker BioSpin GmbH, Ettlingen, Germany).

2.6.2. Cell culture. Human cervical carcinoma cells (HeLa) were used to test the toxicity of the different nanostructures synthesized and the commercial CAs. The cell line was obtained from the American Type Culture Collection (ATCC; Manassas, VA, USA) and maintained in MEM Alpha medium (Invitrogen) supplemented with 10% (v/v) heat inactivated fetal bovine serum (FBS) and incubating them at 37 ^{o}C under atmosphere with 95% humidity and 5% CO_2.

2.6.3. Cell viability studies. HeLa cells in logarithmic growth phase were seeded by adding 3000 cells/well in 100 μL final volumes in 96-well microplates. After 24 h, cells were treated with increasing doses of the NCPs or commercial CAs based on Gd (Gadopentetate dimeglumine, GdDTPA, Guerbet, Roissy, France) and Mn (Mangafodipir trisodium, MnDPDP, Bayer Healthcare). The effect on cell viability after 24h and 72h was determined using the PrestoBlue reagent assay, which is based on the metabolic reduction of resazurin on resorufin. A Victor3 (Perkin Elmer) fluorimeter plate reader was used to obtain the measurements by fluorescence reading directly from 96-well microplates at an excitation wavelength of 531 nm and emission wavelength of 572 nm. The percentage of cell viability was calculated by dividing the absorbance of each well by the corresponding value of the control wells (cells without treatment). The cytotoxicity studies were carried out by triplicate and a minimum of four independent experiments performed on different days. The data was treated with GraphPad Prism software (Version 4.0).

2.6.4. Intracellular reactive oxygen species (ROS) generation studies. Measurement of intracellular ROS activity was based on fluorescence emission measurements using CellRox Green Reagent (Molecular Probes). HeLa cells were seeded in 96-well microplates allowed to attach and grow during 24 h. After this time, cells were treated 24 h more with NCPs or commercial CAs. Finally, 20 µL of CellRox reagent was added to each well and incubated for 30 min. Two controls were made: one with cells treated only with cell culture medium as a reference value, and second with H_2O_2 (as an oxidative stress inducer for positive control). The measurements were recorded at an excitation wavelength of 485 nm and emission wavelength of 535 nm using a Victor3 (Perkin Elmer) fluorimeter.

2.7. *Ex vivo*/*In vivo* assays

2.7.1. Animal models. Animal studies were approved by the local ethics committee, according to the regional and state legislation (protocol DMAH-8333/CEEAH-2785). C57BL/6J female mice of 12 weeks of age, weighting 21.4 ± 1.2 g (n = 12) were purchased from Charles River Laboratories (l'Abresle, France) and housed in the animal facility of the *Universitat Autònoma de Barcelona*. For *ex vivo* studies, control C57BL/6J mice were used. For *in vivo* studies, GL261 tumor-bearing mice were used, except for tolerability evaluation.

2.7.2. MRI Studies. All MRI studies were performed at the joint nuclear magnetic resonance facility of the *Universitat Autònoma de Barcelona* and *Centro de Investigación Biomédica en Red – Bioingeniería, Biomateriales y Nanomedicina* (CIBER-BBN) (Cerdanyola del Vallès, Spain), Unit 25 of NANBIOSIS, www.nanbiosis.es. The 7T Bruker BioSpec 70/30 USR spectrometer (Bruker) equipped with a mini-imaging gradient set (400 mT/m) was used for MR acquisitions.

2.7.3. MRI *ex vivo* studies. The CAs were dispersed in 2 ml PBS added with 0.5 mM BSA. The final amount used for each animal was 5 nmol of metal dissolved in 4 µl PBS - BSA solution. Commercial solutions of CAs based on Gd (GdDTPA) and Mn (MnDPDP) were used as standards to compare the enhancement obtained with the NCPs synthesized. Three injection points were used in each mouse (n = 2 for each CA). High resolution T_{1w} and T_{2w} MR images (TR/TE =4200/12 ms) were acquired using a rapid acquisition with relaxation enhancement (RARE) sequence for a morphological characterization of the investigated tissue. All the CAs administrations were done *post mortem* using a stereotactic holder.

2.7.4. Tolerability Studies. Increasing amounts of Fe-NCP (0.03 to 0.4 mmol Fe Kg^{-1}) were intravenously (i.v.) administered to n = 3 mice with a 2-day rest period between injections. An additional group of n = 3 wild type (wt) mice was injected with the vehicle for *in vivo* studies (PBS + 0.5 mM of MSA). Mice body weight and other welfare parameters were followed up for detection of any signs of animal suffering during 30 days after the last administration. No higher doses were tested in this assay.

2.7.5. MRI *in vivo* studies. GL261 tumor-bearing mice (n = 3, 12.7 ± 0.6 days after tumor implantation, tumor volume 38.1 ± 27.5 mm^3) were placed in a mouse bed and anesthetized with isoflurane 0.5–1.5% in O_2. Breathing (60-80 breaths/min) and temperature (37-38 °C) were constantly monitored (SA Instruments, Inc., New York, USA). A first experiment with commercial GdDTPA administration was carried out. A second experiment with Fe-NCP was performed with n = 3 mice. The amount of CA injected in tumor-bearing mice was 107.1 ± 6.4

µl (0.4 mmol metal kg^{-1}). In order to assess both T_1 and T_2 RCE, $T_{1\mathrm{w}}$ and $T_{2\mathrm{w}}$ images (TR/TE = 200/8.5 ms and 4200/12 ms, respectively) were acquired before and immediately after i.v. injection of CA. Three $T_{1\mathrm{w}}$ and three $T_{2\mathrm{w}}$ images were acquired before the CA injection. Then, alternated $T_{1\mathrm{w}} – T_{2\mathrm{w}}$ images were acquired continuously during 30 min after CA administration, resulting in a total of 15 frames for $T_{1\mathrm{w}}$ and 15 frames for $T_{2\mathrm{w}}$ images. In addition, individual $T_{1\mathrm{w}}$ and $T_{2\mathrm{w}}$ acquisitions were also performed at 2 and 24 h after CA administration. Studies were also conducted (n = 3) with the vehicle of administration (PBS-MSA) with a standard DCE-MRI sequence consisting in $T_{1\mathrm{w}}$ MRI acquisitions in a total of 70 frames, with no T_2 alternating sequences.

2.7.6. Processing and post-processing of MR data. For *ex vivo* studies, ROIs were selected in $T_{1\mathrm{w}}$ and $T_{2\mathrm{w}}$ images, corresponding to the CAs administration points. They were manually defined after visual inspection in the area of maximum enhancement and an equivalent area of contralateral parenchyma. The relative contrast enhancement (RCE) - injection site ROI vs. contralateral parenchyma - obtained in each case was used for calculations (see Equation 1). Only the slice with better defined contrast-enhanced region in the best study was used for measurements. For dual enhancement images, $T_{1\mathrm{w}}$ and $T_{2\mathrm{w}}$ images were processed with the algebra algorithm (MR signal T_1 /MR signal T_2) provided by Paravision 5.1.

$$\mathrm{RCE}(\%)_{ex\ vivo} = \left(\frac{S_{(i)}}{S_{(c)}}\right) \mathrm{x}\ 100 \qquad \text{(Equation 1)}$$

Where S(i) is the absolute signal intensity of the “ipsilateral” region with respect to the contrast administration (visually shows contrast enhancement) and S(c) is the absolute signal intensity of the equivalent contralateral region.

For *in vivo* studies, two ROIs were manually selected in each slice: one corresponding to the tumor area and the second corresponding to contralateral normal brain tissue. Then, RCE for each slice was calculated as in *ex vivo* studies. Mean RCE of the three images acquired before CA injection was referred as 100%, and then RCE signals of images acquired after CA injection were estimated accordingly.

2.8. Statistical analysis. Normality of the distribution values was inspected with Kolmogorov-Smirnov test. Variance equality was estimated with Levene's test. Student's t-test was used for RCE bilateral comparisons. The *in vitro*, *ex vivo* and *in vivo* RCE evolution during the first 30 minutes was performed with UNIANOVA. Significance level was set to 0.05.

2.9. Biodistribution studies. ICP-MS was used for the biodistribution of Fe-NCP. For each experimental group, prior to injection, a nanoparticle aliquot was saved for the determination of iron concentration in the injected material. After the *in vivo* experiments, the mice were euthanized and the organs of interest (brain, tumor, lungs, bladder, kidneys and liver) excised and stored at -80 ºC. Previous to ICP-MS measurements, organ samples were thoroughly washed with PBS and blotted dry to minimize the contribution of any nanoparticles still circulating in the blood. The organs were weighted into vials and digested overnight at 70 ºC with 1 ml of protein extraction reagent (T-PER™, Thermo Fisher Scientific) per 100 mg of tissue and 10 mL of aqua regia ($1HNO_3$:3HCl, trace metal grade) (v/v). After that, the organs were sonicated with an ultrasounds probe (Branson 550, Emerson, St Louis, MO, USA) for 10 cycles until the complete digestion (300 W, 10 min). For the quantification of metal a dilution 1:100 was necessary for detecting the correct signals. For ICP-MS analysis, atomic spectroscopic analytical standards were purchased from PerkinElmer Pure Plus. The isotope ^{57}Fe was selected as tracer. The iron concentration of each sample was measured using a calibration curve obtained in the range of 0.01-500 ppb of metal. Standard reference material (PerkinElmer) with known values of Iron was analyzed with each batch of samples. All the samples were measured per quadruplicate. For protein quantification a Bradford kit protocol was used (Quick Start Bradford Dye reagent X1, Biorad, Hercules, CA, USA). The biodistribution of iron ions was plotted per μg of protein content in each organ. The results were expressed as mean ± SD. An unpaired Student's t-test was used. Significant level was set to 0.05.

3. Results and Discussion

3.1 Synthesis and characterization of NCPs

The synthesis of NCPs containing three different paramagnetic ions widely used as CAs for MRI (Fe^{3+}, Gd^{3+} and Mn^{2+}) was achieved. The NCPs where synthesized using a previously published methodology[40] through the reaction of $Fe(CH_3COO)_2$, $Gd(CH_3COO)_3 \cdot 6H_2O$ or $Mn(CH_3COO)_3$ metal salts with 1,4-Bis(imidazole-1-ylmethil)-benzene (L1, Bix) and 3,4-dihydroxycinnamic acid (L2, dhc) as a co-ligand in a 1:1:2 molar ratio, and using EtOH as solvent. These reactions afforded the formation of the nanoparticles named Fe-NCP, Gd-NCP and Mn-NCP, respectively. Alternatively, the polymerization of the well-known commercial CA for MRI based on Gd (Gadopentetate dimeglumine, GdDTPA) was tested in similar way by mixing $Gd(CH_3COO)_3 \cdot 6H_2O$ with L1 and diethylenetriaminepentaacetic acid (L3, DTPA) as a co-ligand (Figure 1a). In a first trial, the idea was to polymerize the commercial GdDTPA chelate using different ligands. However, all the attempts to obtain this coordination polymer were unsuccessful. For this reason, the formation of the chelate and subsequent polymerization process was performed *in situ* as detailed in the Experimental section. In the same way, polymerization of the Manganese-based commercial CA (Mangafopidir trisodium, MnDPDP) was attempted. Nevertheless, the resulting polymer showed low reproducibility and low chemical stability in aqueous solution and, for this reason, the system was discarded.

All the NCPs were characterized by SEM, showing different diameter size ranging from 45 ± 5 nm (Fe-NCP) to 130 ± 7 nm (Mn-NCP) (Figure 1b-e and Table 1). In solution, DLS measurements in PBS buffer show higher hydrodynamic diameters in comparison with SEM measurements. In general, good monodispersion values (PDI < 0.20) and colloidal stability are found for all samples, except for the Mn-based NCP (Mn-NCP), which start to aggregate in a relatively short time (sedimentation observed after 1 h). This aggregation process can be related to the surface charge or the low chemical stability of the nanoparticles. Indeed, the ξ-potential measurements show strong negative values for Iron and Gadolinium-based NCPs (-31.2 and -27.2 mV, respectively). Otherwise, Mn-NCP shows weaker ξ-potential values (-15.4 mV) inducing low electrical repulsion between the nanoparticles (Table 1). With the aim to mimic the physiological environment and improve the colloidal stability of the NCPs, the nanoparticles were dispersed in a solution containing PBS and BSA (0.5 mM) at physiological conditions.[41,42] The results obtained demonstrate an improvement on the dispersions and colloidal stability of the NCPs in aqueous media, reducing the visible aggregation and showing hydrodynamic diameters close to the mean size values obtained by SEM (see Table 1 and Figure S1a-b).

The chemical characterization of the resulting nanoparticles was performed by different complementary techniques. The FT-IR spectroscopy for Fe/Gd/Mn-NCPs shows the disappearance of the bands corresponding to the catechol –OH groups of L2 in the range of ν = 3000-3500 cm^{-1}, reflecting their deprotonation. Moreover, the vibration band assigned to a C–O stretch for the catechol coordinated to the metal appears in the frequency range 1400-1420 cm^{-1}. The prevalence of carboxylic acid groups is confirmed by the presence of the characteristics vibrational bands of C=O and C–OH in the range ν = 1650-1580 cm^{-1} and 1250-1200 cm^{-1}, respectively. Additionally, typical vibrational bands of L1 (ν = 1520, 1232, 1105 cm^{-1}) are observed in the IR spectra (Figure S2a-d). In the specific case of GdDTPA-NCP, the coordination of the carboxylic groups to Gd^{3+} ions, is confirmed by the presence of the characteristics vibrational bands of the COO^{-} carboxylate group at $\nu = 1590\ cm^{-1}$ and $\nu = 1380\ cm^{-1}$.

The FT-IR spectra comparison between GdDTPA-NCP complex and the Gd commercial CA (GdDTPA), reflects a good agreement on GdDTPA related signals and the presence of the additional peaks corresponding to the Bix (L1) ligand used as linker between metal centers (Figure S2d). The XPS measurements, confirm the presence and oxidation state of the metals being Fe(III), Gd(III) and Mn(II) in each case (Figure S3a-e). Additionally, Mössbauer spectroscopy confirms that Fe-NCP show a high-spin Fe(III) oxidation state (Figure S4). The chemical compositional formula of different complexes was experimentally calculated by combination of ^{1}H-NMR, ICP-MS and elemental analysis. The ligand ratio of NCPs was obtained from ^{1}H-NMR and the metal percentage from ICP-MS (Table S1-S2). These results together with the elemental analysis of C, N and H, help to elucidate an average compositional formula (the experimental compositional formulas for each NPC complex are shown in the Experimental section). As the NCPs are obtained out of equilibrium, it is worth mentioning that elemental analysis of different nanoparticles batches slightly differ from the expected values for a 1(metal ion):1L1:2L2 (or L3) ratio. These differences have been tentatively attributed to the plausible encapsulation of free ligand or solvent molecules within the particles and the formation of secondary structures such as oligomers.[43,44] Finally, the absence of diffraction peaks observed by powder X-ray diffraction (PXRD) indicates the amorphous nature of all the samples. (Figure S5)

3.2 Biodegradability of NCPs

The size and the surface ξ-potential of the NCPs were studied at different pH in aqueous media (PBS buffer). In acidic media (pH < 4), the protonation of the carboxylic acid, and the consequent reduction of ξ-potential, induces the aggregation and precipitation of the nanoparticles. On the other hand, the lowest particle size value is obtained at pH = 9 in which a high percent of carboxylic groups are deprotonated and the surface charge is highly negative resulting in less aggregation due to electrostatic repulsion between nanoparticles (Figure S6-S7). For values below pH = 4 or above pH = 9, the decomposition of the polymeric material becomes evident due to the complete and irreversible dissolution of the nanoparticles within a few seconds. In order to evaluate the colloidal and chemical stability of the nanoparticles in physiological conditions, dispersions of specific concentrations of the different NCPs were followed for 24 h and 48 h. In a typical experiment, the nanoparticles were placed inside a dialysis bag immersed in a PBS buffer solution at pH = 7.4 and 37 ^{o}C. The chemical stability of the NCPs was studied by FT-IR spectroscopy (Figure S8a-d) and the liberation of metal, most likely arising from degradation of NCPs, was quantified from outside the dialysis bag using ICP-MS spectrometry (Figure S9a-b and Table S3). The results indicate a gradual biodegradation for Fe-NCP which reached the 50% metal leaching after 8 h. The Gd-NCP nanoparticles, and specially Mn-NCP, were less stable taking into account their decomposition rates showing significant leaching (50% at 5 h and 2 h for Gd-NCP and Mn-NCP, respectively). In the case of GdDTPA-NCP, although the chemical stability is maintained up to 6 h, the degradation turn evident for longer times by the successive disappearance of vibrational bands due to the chemical decomposition (Figure S8d). In the same way, chemical degradation is observed when UV-vis spectra are recorded at different times for the different systems in solution. The degradation of the nanoparticles and metal release are associated with the significant appearance of absorption bands in the wavelength range 400-600 nm, which correspond to the absorption of soluble metal complexes in solution (Fe(III) at 590 nm after 24 h, Gd(III) at 450 nm after 12 h, Gd(III)DTPA at 550 nm after 12 h and Mn(III) at 450 nm after 4 h) (Figure 2, Table S4). Considering those results, a notably better stability of Fe-NCP in comparison to the other nanoparticles is corroborated. This result confirms what was previously expected, since the constant stability of metal-catechol complexes depends on the hardness character of the metal. In the case of Fe(III)-catecholate complexes, the stability constants are extremely high compared with the Gd(III) and Mn(II) derivatives.[45,46] Previous studies corroborate that Fe(III)-catechol complexes possess unique combination of mechanical features including high mechanical stability, fast reformation kinetics, and environmental sensitive mechanics.[47] In basis of these results, the stability of Fe-NCP is enough for the MRI acquisition, without accumulation within the organism avoiding undesirable side effects.

3.3 Biocompatibility: cytotoxicity assays and reactive oxygen species (ROS) generation

The biocompatibility of NCPs using *in vitro* viability assays on HeLa (human cervix carcinoma) cells was evaluated after 24 and 72 h incubation with different concentrations of NCPs. As shown in Figure 3a, after 24 h, iron and gadolinium-based NCPs do not show significant toxicity at metal concentrations up to 100 μM, meanwhile manganese-based NCPs showed a notable toxicity just above 10 μM. At highest concentrations (200 μM) and longest incubation times (72 h) only the Fe-based NCPs do not show toxicity (Figure 3b) in comparison with Gd- and Mn-NCP. Comparatively, the toxic effect of these two last complexes is very similar to the commercial gadolinium (GdDTPA) and manganese (MnDPDP) contrast agents, respectively (Figure S10).

One explanation for the toxicity detected can be attributed to the generation of reactive oxygen species (ROS). It is well known that many of the heavy metal ions can induce the generation of reactive radicals and cause cellular damage via depletion of enzyme activities through lipid peroxidation and reaction with nuclear proteins and DNA.[48,49] The production of ROS induced by nanomaterials plays a vital role in genotoxicity and oxidative DNA damage involving mutagenesis, carcinogenesis and aging-related diseases.[50]

Particularly, metal-based nanoparticles can induce toxicity due to the ionic species generated from nanomaterial dissolution in a suspending medium or a biological system. In this sense, different studies were carried out by incubation of HeLa cells for 24 h with different concentrations of nanoparticles from 0 to 200 μM (based on metal concentration) and using 1 mM H_2O_2 as a positive control for the ROS generation (Figure 3c). All results were compared with the GdDTPA and MnDPDP CAs (Figure 3d). If the production of ROS by the different nanoconstructs is compared with their cytotoxic effect, there is a strong correlation between cell viability and ROS production. Thus, meanwhile Fe-NCP induces a low production of ROS in a dose-dependent manner even for high concentrations, the Gd-based NCPs has an increased ROS generation especially at concentrations higher than 100 μM. The most dramatic response corresponds to the Mn-NCP which presents a notable ROS production above 25 μM. Since most of the examples of metal-induced ROS production are related to the presence of redox-active metals in solution, it is interesting to mention that the appearance of a band at 450 nm during the degradation of Mn-NCP indicates the oxidation of Mn(II) to Mn(III).[51] This fact would justify the increased toxicity observed with this system since Mn(III) results in higher oxidative reactivity in comparison with Mn(II) analogous.[50]

As observed in the previous studies, the chemical stability in aqueous solution of the different NCPs can be stated in the following order: Fe-NCP>Gd-NCP>GdDTPA-NCP>Mn-NCP that interestingly matches with the increasing order of cytotoxicity effect.

3.4 Relaxivity properties of NCPs: in vitro and ex vivo MRI studies

3.4.1 *In vitro*

To evaluate the feasibility of NCPs synthesized as a platform for MRI, the longitudinal (r_1) and transversal (r_2) relaxivity values were determined by T_{1w} and T_{2w} images acquisition for all the dispersions containing the samples at different metal concentrations. For this, the NCPs were redispersed in PBS - agarose 1% solution at pH = 7.4 and measured (representation of R_1, R_2 vs [metal] are shown in Figure S11a-f). As shown in Figure 4a-d, all the samples display a T_{1w} signal enhancement with the increase of the metal ion concentration. The obtained r_1 and r_2 values are summarized in Table 2 (graphical changes on r_1 and r_2 are shown in Figure S12a). The r_1 values were determined to be 5.3 ± 0.1 mM^{-1} s^{-1} for Fe-NCP, 4.4 ± 0.2 mM^{-1} s^{-1} for Gd-NCP, 4.5 ± 0.4 mM^{-1} s^{-1} for GdDTPA-NCP, and 3.7 ± 0.1 mM^{-1} s^{-1} for Mn-NCP. The values obtained are comparable with the commercial GdDTPA (4.4 ± 0.7 mM^{-1} s^{-1}) except for the Fe-NCP complex which significantly improves the referenced value. Concerning the T_{2w} MR images, clear differences are found. In Fe-NCP, the T_{2w} MR image intensity decreases (Figure 4a) with a concentration increase of Fe ions. Thus, the r_2 value for Fe-NCP is 10.9 ± 0.3 mM^{-1} s^{-1}, which is about twice higher than the corresponding commercial GdDTPA (r_2 = 4.6 ± 0.2 mM^{-1} s^{-1}). This increased value is ascribed to the combined effects of the local inhomogeneous magnetic fields created by the NCPs and the exchange of water between NCPs and the environment.[53,54]

The MR behaviour of contrast agents relies on the relaxivity ratio (r_2/r_1). If the material behaves as a T_2 contrast agent, $r_2/r_1 \geq 10$ and as T_1 contrast agent if $r_2/r_1 < 2$.[55] Therefore, nanoparticles with an intermediate r_2/r_1 ratio can be excellent candidates as T_1/T_2 DMCAs. In our case, the *in vitro* phantom imaging studies are in agreement with this assumption for Fe-NCP, since the relaxivity ratio r_2/r_1 is 2.1, indicating its potential use as DMCA. The r_1 value of Fe-NCP is comparable or even higher than those found for previously reported iron-based coordination polymers,[56,57] or molecular complexes,[58] which exhibit r_1 values up to 3.0 mM^{-1} s^{-1}. Such good response is directly related to the Fe-NCP capacity to modify the relaxation times of the water protons in the surrounding medium when a magnetic field is applied. On the one hand, it has been reported that catechol-based ligands maximize second-sphere interactions with water molecules, and therefore to enhance T_1, through hydrogen bonding with the oxygen atoms of the Fe–O–R linkages.[59] On the other hand, the coordination polymer probably contains water molecules strongly coordinated to the metal sites, as well as free water molecules. These labile water molecules are probably in exchange with bounded water molecules, diffusing through the polymeric matrix.[60] The mobility of the metal coordinated water in the first and second coordination spheres should induce an effect on the relaxation times of the water protons, resulting on the observed ratio r_2/r_1.

In the case of gadolinium-based nanoparticles (Gd-NCP and GdDTPA-NCP) although they perform satisfactorily as T_1 CAs, no significant effect as T_2 CA is detected and the r_2 values obtained (4.9 ± 0.2 mM^{-1} s^{-1} and 5.1 ± 0.3 mM^{-1} s^{-1}, respectively) are comparable to the commercial GdDTPA complex (4.6 mM^{-1} s^{-1}) resulting in $r_2/r_1 \sim 1$ ratio. The same trend is observed for Mn-NCP, which shows a typical behaviour of a T_1 contrast agent with $r_2/r_1 = 0.6$ ratios exhibiting value comparable to the Mn-based commercial MnDPDP CA ($r_1 = 3.1 \pm 0.5$ mM^{-1} s^{-1}, $r_2 = 2.3 \pm 0.1$ mM^{-1} s^{-1}).

3.4.2 *Ex vivo*

Before performing *in vivo* studies, it is necessary to select the appropriate candidate which produces the best relative performance in a tissue-like environment.[61,62] Although *in vitro* T_1 and T_2 relaxivity times were calculated, the results obtained from them are not usually comparable in real tissue. Most of the *in vitro* strategies used to evaluate the CAs performance, are not able to reproduce the *in vivo* conditions that could modify their ability to generate contrast.[63-65]

For these reasons, *ex vivo* studies were conducted essentially as reported previously.[62] Briefly, each contrast NCPs was added to a PBS-BSA solution (1.25 μM in terms of metal concentration) and 4 μl of the resulting dispersions were intracranial administered *post mortem* to euthanized mice. The relative contrast enhancement (RCE values) was calculated for each CA. In this case, RCE values give information about the contrast improvement of an administered CA in comparison with the cerebral area without CA injected. A solution of commercial GdDTPA CA was used for comparison purposes (more details about protocol can be found in Experimental section). For statistical reasons, three ROIs were selected in T_{1w} and T_{2w} images, corresponding to CA administration points (Figure 4e-f). The T_{1w} and T_{2w} RCE calculated for each studied CA and vehicle are shown in Table 2 (graphical changes on T_1 and T_2 are shown in Figure S12b). Fe-NCP and Gd-NCP presents RCE T_1 comparable with the two commercial CAs GdDTPA and MnDPDP (with no significant differences). Mn-NCP produces poorer and non-reproducible results presumably due to the low stability of these nanoparticles in solution. Regarding RCE T_2, Fe-NCP presented the best T_{1w}/T_{2w} result, although significance is only reached in comparison with commercial MnDPDP, probably due to high value dispersion. The dual potential of this CA is more clearly observed when the calculated ratio of RCE T_1/T_2 is considered. Ideally, a DMCA should present high absolute values for RCE T_1 (signal increase) and low absolute values for RCE T_2 (signal decrease), resulting in a high RCE T_1/T_2 ratio, as observed for Fe-NCP (RCE

T_1/T_2 = 7.7) (Table 2). In this case, the *ex vivo* studies validate the enhanced performance described *in vitro* for Fe-NCP. Additionally, the low toxicity and high chemical stability make this iron-based complex the best candidate for its preclinical study.

3.5 In vivo MRI studies: tolerability, MRI imaging and biodistribution

3.5.1 Tolerability

Previous to *in vivo* assays, a tolerability study to determine the maximum safe dose for Fe-NCP complex was done. The study was carried out following a protocol adapted and previously reported.[66,67] In a typical experiment, increasing amounts of Fe-NCP (0.03 to 0.4 mmol Fe kg^{-1}) were i.v. administered (via tail vein) to n = 3 mice with a 2-day rest period between injections. An additional group of 3 mice was injected with the vehicle as control (PBS with 0.5 mM Mouse Serum Albumin (MSA)). Mice body weight and other welfare parameters were followed for 30 days after the last administration. In these conditions, a dose of 0.4 mmol $kg^{-1}$of Fe-NCP proved safe and no body weight loss or toxicity symptoms observed during injections and for the 30-day period after the last administration (Figure S13). This value perfectly matches safety administration ranges for Fe- based nanoparticles, which can be up to 0.6 mmol kg^{-1}.[68-71] This is a clear added value of Fe-NCP in comparison with Gd-based contrast agents, which are widely used in clinical practice but are not exempt of undesired effects.[72]

3.5.2 MRI studies

For the *in vivo* CAs study, GL261 glioblastoma tumor-bearing mice were i.v. injected with 107.1 ± 6.4 µl containing the equivalent dose of 0.4 mmol metal kg^{-1}. The commercial GdDTPA CA was administered first, as reference for direct comparison (the complete description of the procedure and acquisition parameters is detailed in Experimental section). Representative T_{1w} (Figure 5a,b) and T_{2w} (Figure 5c,d) images were acquired pre- and post- CA injection.

In a second experiment, Fe-NCP was administered and T_{1w} and T_{2w} images acquired. Consequently, dual enhancement images were obtained through a post-processing algebra algorithm application (T_{1w}/T_{2w}, Figure 5e,f). The RCE values (Table 3) were calculated by manual selection of two ROIs in each MRI slice: one corresponding to the tumor region and a second one to the contralateral normal brain tissue (Figure 5). In this case, the RCE values give information about the contrast improvement before (normalized as 100%) and after CA injection.

Maximum T_1 RCE signal increase (T_{1max}), shows remarkable differences between commercial GdDTPA (250.9 ± 3.1% at 6.1 ± 1.1 min) and Fe-NCP (317.4 ± 9.4% at 9.4 ± 1.1 min), which is notably superior ($p<0.05$). In T_{2w} images, no minimum signal decrease (and accordingly no T_{2min}) is observed for GdDTPA, which even show a slight signal increase (106.8 ± 2.9% at 2.6 ± 1.1 min). However, Fe-NCP shows a notable T_{2w} signal decrease with the minimum mean RCE value observed (73.7 ± 14.4%, with 26% decrease) at 5.3 ± 1.1 min. Significant differences are observed for RCE T_1 curves of GdDTPA, Fe-NCP and vehicle (Figure S14a-b and S15). Additionally, the basal RCE values for Fe-NCP are completely recovered after 24 h and 30 min post-injection for T_1 and T_2, respectively. These values confirm the rapid biodegradability of Fe-NCP and its potential as DMCA for MRI (see Figure 5f where RCE T_1/T_2 ratio is shown). It is worth noting that for Fe-NCP, the T_{1max} is observed at 9.4 ± 1.1 min, meanwhile for the commercial CA the maximum is achieved at 6.1 ± 1.1 min. This difference may be related to the greater retention and accumulation of the nanostructured material due to the enhanced permeability and retention effect (EPR) of nanoparticles in tumors as described in previous works.[65] In our case, the Fe-NCP nanoparticles are able to produce T_1 and T_2 RCE at reasonably short times in the preclinical glioblastoma model (between 3.95 and 10.72 min after administration for maximum T_1/T_2 effect). This behaviour would be a clear advantage, allowing the acquisition of both data types (T_{1w} and T_{2w}) in the same exploration, instead of performing two explorations with a large interlude. Thus, these nanoparticles present a clear interest for future studies, bearing a strong translational potential. This is not restricted to contrast enhancement, as they could be also used as nanocarriers for tumor-drug release and therapy in addition to diagnosis.[73,74]

3.5.3 Biodistribution

To further verify the biocompatibility studies and *ex vivo*/*in vivo* properties as MRI CAs, the biodistribution of Fe-NCP nanoparticles was studied. The quantification of Fe^{3+} levels within the different organs was determined by using ICP-MS. In Figure 6, the biodistribution of iron from Fe-NCP in the main organs, including the tumor, is shown. The results are based on the quantification of µg Fe mg^{-1} protein at 2 min and 24 h after injection of two different Fe-NCP doses (0.2 mmol Fe kg^{-1} and 0.4 mmol Fe kg^{-1}). The experimental results indicate a dose-dependent biodistribution. On the one hand, the very short-term biodistribution (2 min) of low doses of Fe-NCP show a low accumulation in heart and bladder, and notable retention in spleen. On the other hand, no increased levels of iron are detected in the tumor and contralateral brain area. However, when increasing the injected dose up to 0.4 mmol Fe kg^{-1}, 2 min of circulation time is enough to observe the presence of Fe-NCP in the brain and tumor. After 24 h, for the low dose administration no increase in the concentration of iron was detected in any organ except spleen. Nevertheless, at high doses, notable accumulation is still observed in tumor, brain and bladder. At the same time, the considerable decrease in concentration observed in heart and the increasing concentration in bladder must be attributed to the decrease of nanoparticles in blood circulation and consequent excretion. The accumulation observed in the lungs, liver and kidneys are negligible and no significant differences were found in comparison with the basal values (control wild type mice). As observed, Fe-NCP results in a minimal tissue accumulation and gradual degradation/excretion without bioaccumulation. These results confirm the rapid excretion of the nanoparticles due to the intrinsic biodegradability of the Fe-NCP complex. Actually, the gradual increase concentration of iron in bladder is an indicative of a gradual biodegradation of the Fe-NCP since the size needed to pass through the kidneys and reach the bladder should be smaller than 8 nm.[75] The large uptake of the Fe-NCP observed in spleen indicates its important role in the nanoparticle pharmacokinetics based on their rapid clearance by the mononuclear phagocytic system (MPS) which is common for unmodified nanoparticles bigger than 40 nm.[76,77] Although the persistence of Fe-NCP in the spleen may arise initial concerns, no adverse effects were detected in the 30 day-long tolerability assays described before.

4. Conclusions

Nanostructured coordination polymers (NCPs) based on Fe^{3+}, Gd^{3+} and Mn^{2+} paramagnetic ions have been synthesized and tested as novel contrast probes with improved features in comparison to commercial CAs. From the different synthesized NCPs, only Fe-NCP shows relevant advantages in terms of: i) Chemical and colloidal stability, low cytotoxicity, and MRI relaxivity results as DMCA; ii) The *in vivo* MRI shows its T_1 and T_2 contrast potential, allowing almost simultaneous recording of positive and negative contrast images in a very short period of time (between 3.95 and 10.72 min after administration for maximal contrast effect); iii) This reduced time is a clear advantage in comparison with other DMCAs previously described, during which the Fe-NCP complex shows a high enough contrast activity for diagnosis and iv) The tolerability and biodistribution assays indicate the persistence of the nanoparticles in the tumor and the gradual clearance through the kidneys denoting the biodegradability of the system. This work will pave the way for development of enabled biodegradable nanoparticles with T_1/T_2 dual-mode MRI contrast enhancement, obtained fast and safely, and which represents a clear advantage in comparison with other DMCAs. Further studies will include the functionalization of the Fe-NCP nanoparticles surface to avoid fast elimination of the CA by the mononuclear phagocytic system (i.e. coating with PEG), and to increase the targeting properties for specific tumors.

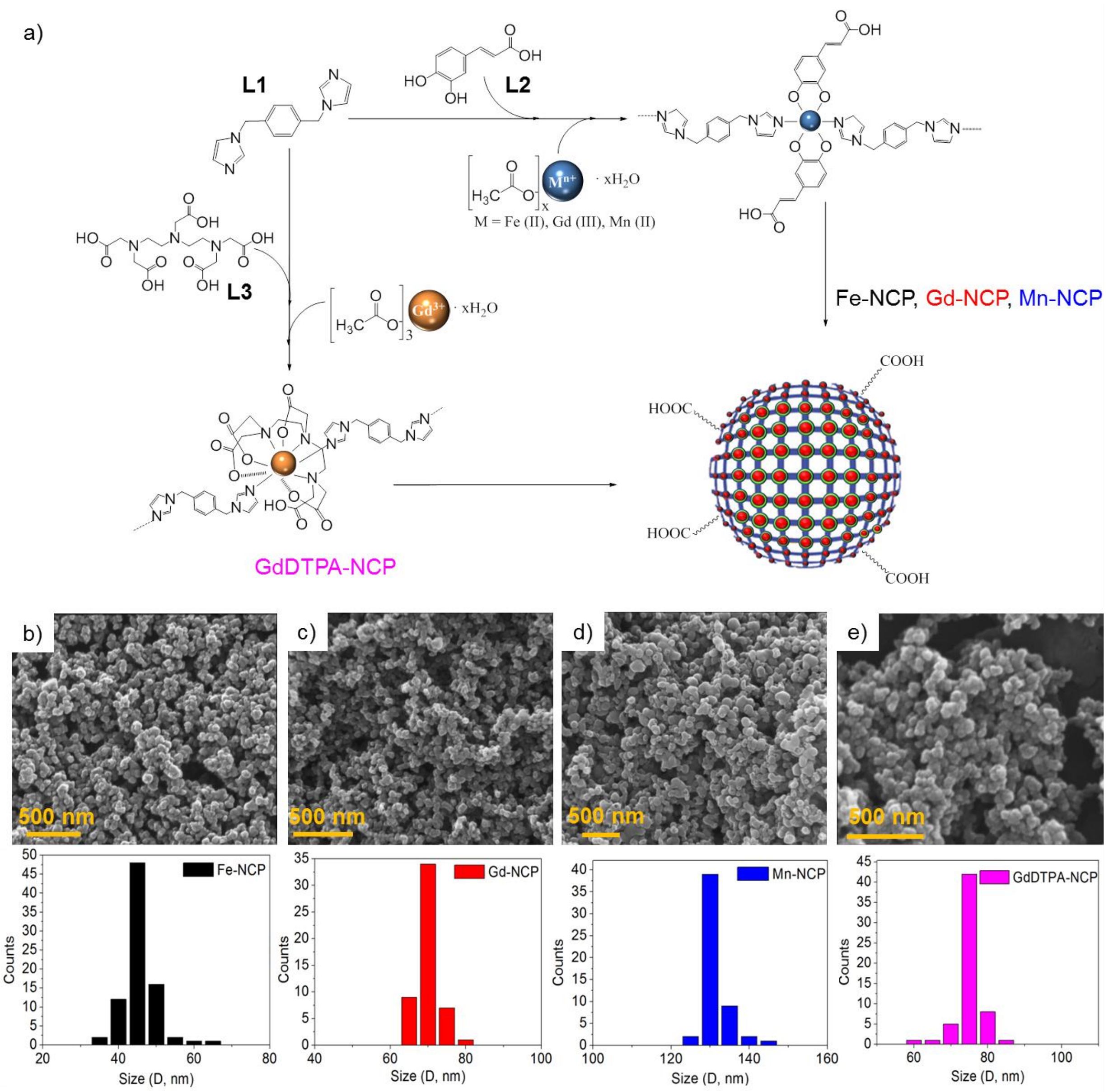

Figure 1. Synthesis and morphology of the NCPs complexes. (a) Scheme for the synthesis of the different NCPs complexes; SEM images for (b) Fe-NCP, (c) Gd-NCP, (d) Mn-NCP and (e) GdDTPA-NCP. Below each SEM image, the corresponding size histogram for each NCP complex is shown.

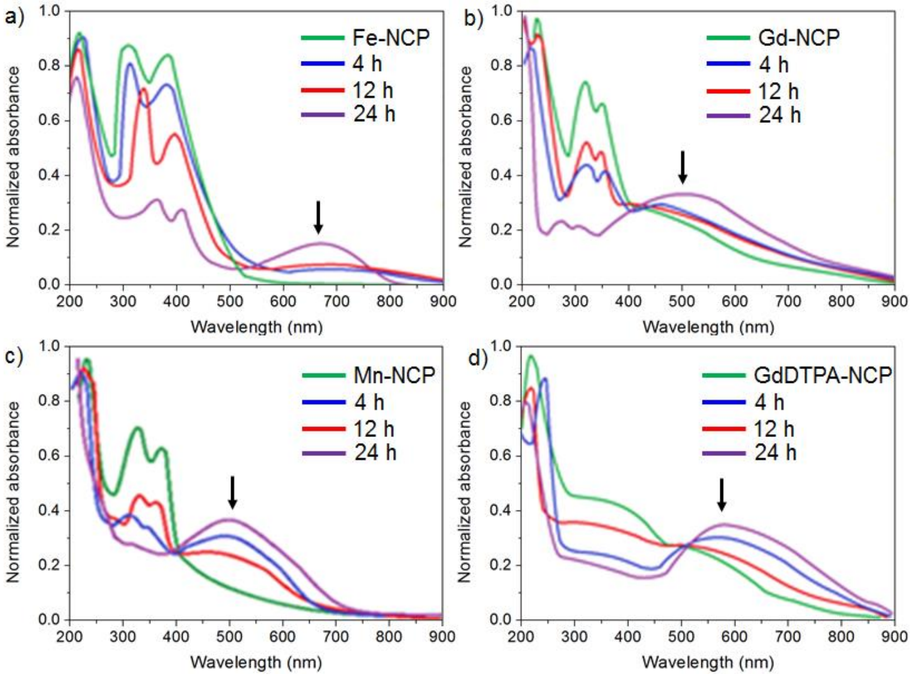

Figure 2. Chemical stability of NCPs. The UV-vis spectra show the biodegradability through the time (4, 12 and 24 h) for (a) Fe-NCP, (b) Gd-NCP, (c) Mn-NCP and (d) GdDTPA-NCP. The arrow indicates the appearance and increase of the band related with the metal release.

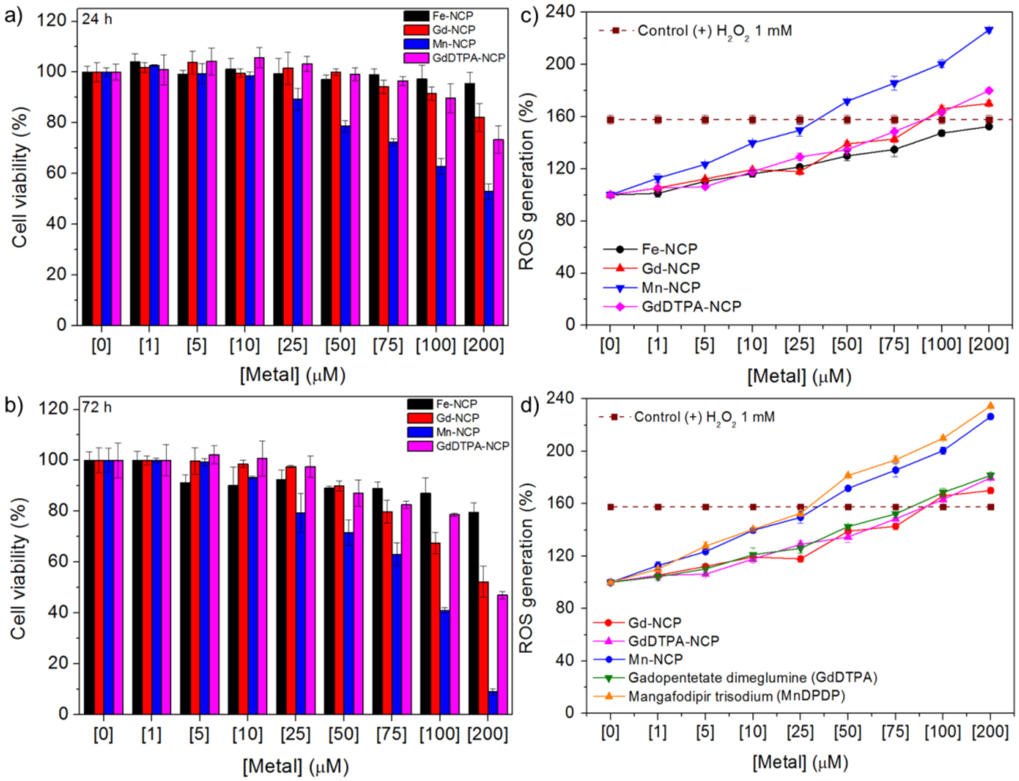

Figure 3. The effect of the NCPs on cell viability and reactive oxygen species (ROS) generation in HeLa cells. Concentration-dependent cytotoxicity effects of NCPs were evaluated after (a) 24 h and (b) 72 h of incubation. The ROS generation was evaluated for 24 h for (c) NCPs and (d) compared with commercial CAs. Data is shown as mean ± standard deviation.

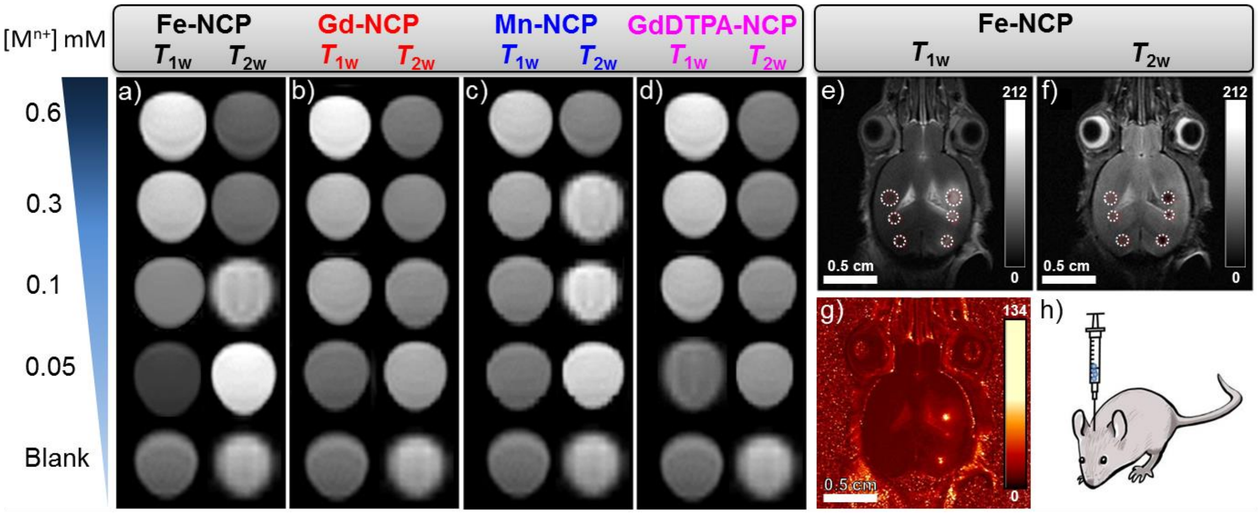

Figure 4. In vitro and *ex vivo* contrast effect of NCPs. Different phantoms series for each NCP complex at decreasing metal concentration: (a) Fe-NCP, (b) Gd-NCP, (c) Mn-NCP and (d) GdDTPA-NCP. The *ex vivo* Fe-NCP (e) T_{1w} and (f) T_{2w} MRI images obtained after stereotactic injection of Fe-NCP, and (g) post-processing of T_{1w} and T_{2w} images by an algebra algorithm of imaging division (T_{1w}/T_{2w}); (h) for the *ex vivo* experiments all NCPs were stereotactically injected in brain parenchyma. The dashed circles show the selection of regions of interest (ROIs) for the relative contrast enhancement (RCE) calculation. Color scales show the range of pixel values in grayscale (for T_{1w} and T_{2w} weighted images) or "*hot metal*" color scale (for double enhancement images T_{1w}/T_{2w}), with minimum and maximum values.

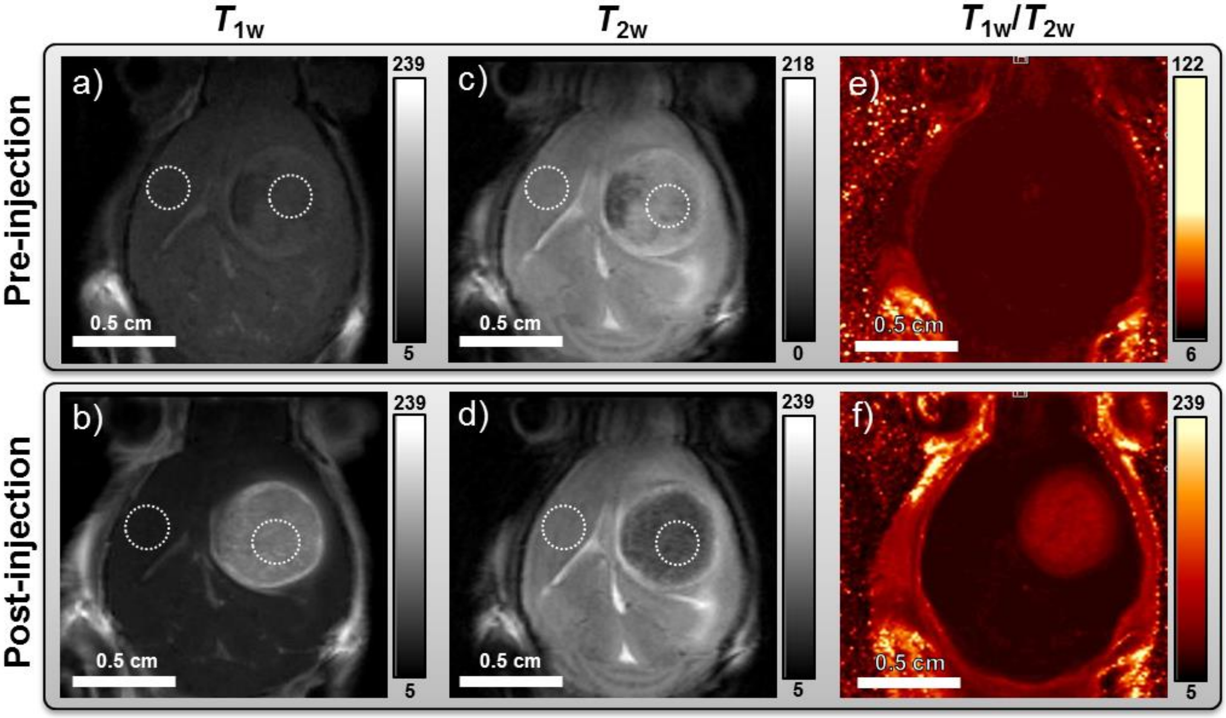

Figure 5. Example of *in vivo* study of GL261 tumor bearing mice (mouse number C1210) administered with Fe-NCP (0.4 mmol Fe Kg^{-1}). In the first row, MR images obtained before injection (pre-injection) are shown: (a) T_{1w} image, (b) T_{2w} image and (c) image obtained from an algebra algorithm of imaging division (T_{1w}/T_{2w}). In the second row, MR images after injection obtained at T_{1max} (post-injection) are shown: (d) T_{1w} image, (e) T_{2w} image and (f) image obtained from an algebra algorithm of imaging division (T_{1w}/T_{2w}). The dashed circles show the selection regions of interest (ROIs) for the relative contrast enhancement (RCE) calculation. Color scales show the range of pixel values in grayscale (for T_{1w} and T_{2w} weighted images) or "*hot metal"* color scale (for double enhancement images T_{1w}/T_{2w}), with minimum and maximum values.

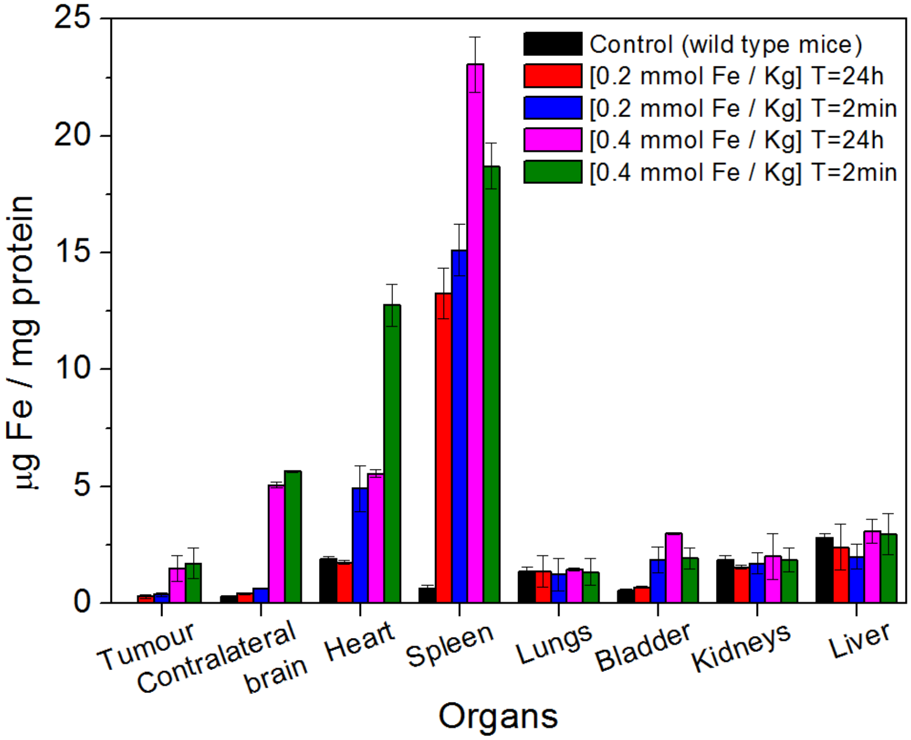

Figure 6. Biodistribution of Fe-NCP in mouse organs. Fe-NCP was injected into mice intravenously with a dosage of 0.2 or 0.4 mmol Fe kg^{-1} body weight. The concentration of Fe in different tissues was detected by ICP–MS at various time points post injection. Data is shown as mean ± standard deviation.

Table 1. Comparison of size distribution (including standard deviation values) and ξ-potential for NCPs in different media.

NCP system	SEM (nm)	PBS		PBS-BSA	
		DLS (nm)	ξ-Pot. (mV)	DLS (nm)	ξ-Pot. (mV)
Fe-NCP	45 ± 5	97 ± 32	-31.2	56 ± 21	-19.1
Gd-NCP	70 ± 3	121 ± 23	-27.2	73 ± 18	-14.7
Mn-NCP	130 ± 7	189 ± 21	-15.4	151 ± 23	-2.2
GdDTPA-NCP	75 ± 8	143 ± 17	-23.9	80 ± 15	-11.9

Table 2. *In vitro* r_1 and r_2 parameters and *ex vivo* relative contrast enhancement (RCE for T_1 and T_2) for all NCPs and comparison with the commercial CAs GdDTPA and MnDPDP.

	In vitro phantoms				*Ex vivo*			
	Medium	r_1 (mM^{-1}s^{-1})	r_2 (mM^{-1}s^{-1})	r_2/r_1	Medium	RCE% (T_1)	RCE% (T_2)	RCE% (T_1/T_2)
Fe-NCP	PBS + Agarose	5.3 ± 0.1	10.9 ± 0.3*$^{¥}$	2.1	PBS + BSA	269.0 ± 28.0	44.9 ± 26.0**	7.7 ± 4.5
Gd-NCP		4.4 ± 0.2	4.9 ± 0.2	1.1		278.6 ± 56.0	70.1 ± 25.4	4.2 ± 1.1
Mn-NCP		3.7 ± 0.1	2.1 ± 0.1	0.6		300.9 ± 47.7	97.4 ± 14.5	3.2 ± 1.1
GdDTPA-NCP		4.5 ± 0.4	5.1 ± 0.3	1.1		180.0 ± 64.3	78.6 ± 2.8	2.3 ± 0.8
GdDTPA		4.4 ± 0.2	4.6 ± 0.7	1.1		253.1 ± 32.8	74.9 ± 17.6	3.6 ± 1.4
MnDPDP		3.1 ± 0.5	2.3 ± 0.1	0.7		300.9 ± 47.7	97.4 ± 14.5	3.2 ± 1.1
Vehicle		-	-	-		118.6 ± 8.8	122.9 ± 11.5*$^{¥}$	0.97 ± 0.07*$^{¥€}$

*= $p<0.05$ in comparison with GdDTPA, MnDPDP, Fe-NCP, Gd-NCP; ¥= $p<0.05$ in comparison with GdDTPA; €= $p<0.05$ in comparison with Mn-NCP; **= $p<0.05$ in comparison with MnDPDP CA.

Table 3. *In vivo* relative contrast enhancement (RCE) for the Fe-NCP complex and the commercial contrast agent GdDTPA.

	In vivo relative contrast enhancement *(*RCE %)					
	T_{1w} (increase)[a]			**T_{2w} (decrease)**[a]		
	T_{1max}	**2 h**	**24 h**	**T_{2min}**	**2 h**	**24 h**
Fe-NCP	317.4 ± 15.4 *** ¥	123.5 ± 4.6 ***	88.3 ± 6.7 ***	73.7 ± 14.4 £,€	103.1 ± 9.9	79.4 ± 4.2 £
GdDTPA	250.9 ± 3.1 *	111.8 ± 2.7 *	101.0 ± 4.0	106.8 ± 2.9 **	102.1 ± 7.0	102.3 ± 7.3
Vehicle PBS-MSA	101.2 ± 1.8					

[a] The 100% RCE is the normalized reference value corresponding to the pre-injection MRI.

*= $p<0.05$ in comparison with GdDTPA RCE T_{1w} pre-injection; **= $p<0.05$ in comparison with GdDTPA RCE T_{2w} pre-injection; ***= $p<0.05$ in comparison with Fe-NCP T_{1w} pre-injection; £= $p<0.05$ in comparison with Fe-NCP T_{2w} pre-injection; ¥= $p<0.05$ in comparison with GdDTPA at T_{1max}; € = $p<0.05$ in comparison with GdDTPA at T_{2min}. If the obtained values ranged >95 to <105% (i.e. less than 5% variation respect to pre-injection), they were considered as “no change” respect to pre-injection.

ASSOCIATED CONTENT

Supporting Information.

Figures S1 to S15 and Tables S1 to S4 are available free of charge on the ACS Publications website. Physicochemical characterization (DLS, FT-IR, XPS, Mössbauer, EA, ICP-MS,PXRD). Colloidal stability (DLS). Chemical stability (FT-IR, UV-vis, ICP-MS). *In vitro* cell viability. *In vitro* MRI. *In vivo* MRI.

AUTHOR INFORMATION

Corresponding Author

* (J. Lorenzo) E-mail: julia.lorenzo@uab.cat

** (F. Novio) E-mail: fernando.novio@icn2.cat

Author Contributions

The manuscript was written through contributions of all authors. All authors have given approval to the final version of the manuscript.

ACKNOWLEDGMENT

This work was supported by the project MAT2015-70615-R and BIO2016-78057-R from the Spanish Government and by FEDER – European Commission funds. ICN2 acknowledges support from the Severo Ochoa Program of the Spanish Ministry of Economy, Industry and Competitiveness (MINECO, Grant SEV-2013-0295). The ICN2 is funded by the CERCA program/Generalitat de Catalunya. MR studies were carried out at the joint NMR facility of UAB and CIBER-BBN, Unit 25 of NANBIOSIS, and time allocation is gratefully acknowledged.

NOTE

The authors declare no competing financial interest.

REFERENCES

1. Weissleder, R.; Ross, B. D.; Rehemtulla, A.; Gambhir, S. S. Molecular Imaging: Principles and Practice. Shelton, CT, USA: People's Medical Publishing House, **2010**.

2. Cabrera-García, A.; Checa-Chavarria, E.; Pacheco-Torres, J.; Bernabeu-Sanz, Á.; Vidal-Moya, A.; Rivero-Buceta, E.; Sastre, G.; Fernández, E.; Botella, P. Engineered Contrast Agents in a Single Structure for T1-T2 Dual Magnetic Resonance Imaging. *Nanoscale* **2018**, *10*, 6349–6360.

3. Li, Z.; Yi, P. W.; Sun, Q.; Lei, H.; Zhao, H. L.; Zhu, Z. H.; Smith, S. C.; Lan, M. B.; Lu, G. Q. Ultrasmall Water-Soluble and Biocompatible Magnetic Iron Oxide Nanoparticles as Positive and Negative Dual Contrast Agents. *Adv. Funct. Mater.* **2012**, *22*, 2387−2393.

4. Na, H. B.; Song, I. C.; Hyeon, T. Inorganic Nanoparticles for MRI Contrast Agents. *Adv. Mater.* **2009**, *21*, 2133–2148.

5. Jun, Y.-W.; Lee, J.-H.; Cheon, J. Chemical Design of Nanoparticle Probes for High-Performance Magnetic Resonance Imaging. *Angew. Chem. Int. Ed.* **2008**, *47*, 5122–5135.

6. Villaraza, A. J. L.; Bumb, A.; Brechbiel, M. W. Macromolecules, Dendrimers, and Nanomaterials in Magnetic Resonance Imaging: The Interplay between Size, Function, and Pharmacokinetics. *Chem. Rev.* **2010**, *110*, 2921–2959.

7. Rogosnitzky, M.; Branch, S. Gadolinium-Based Contrast Agent Toxicity: a Review of Known and Proposed Mechanisms. *Biometals* **2016**, *29*, 365–376.

8. Ramalho, J.; Semelka, R. C.; Ramalho, M.; Nunes, R. H.; AlObaidy, M.; Castillo, Gadolinium-Based Contrast Agent Accumulation and Toxicity: An Update. *AJNR Am. J Neuroradiol.* **2016**, *37*, 1192–1198.

9. Lee, N.; Hyeon, T. Designed Synthesis of Uniformly Sized Iron Oxide Nanoparticles for Efficient Magnetic Resonance Imaging Contrast Agents. *Chem. Soc. Rev.* **2012**, *41*, 2575–2589.

10. Hasebroock, K. M.; Serkova, N. J. Toxicity of MRI and CT Contrast Agents. *Expert Opin. Drug Metab. Toxicol.* **2009**, *5*, 403–416.

11. Khawaja, A. Z.; Cassidy, D. B.; Al Shakarchi, J.; McGrogan, D. G.; Inston, N. G.; Jones, R. G.; Revisiting the Risks of MRI with Gadolinium Based Contrast Agents-Review of Literature and Guidelines. *Insights Imaging* **2015**, *6*, 553–558.

12. Kanal, E.; Tweedle, M. F. Residual or Retained Gadolinium: Practical Implications for Radiologists and Our Patients. *Radiology* **2015**, *275*, 630–634.

13. McDonald, R. J.; McDonald, J. S.; Kallmes, D. F.; Jentoft, M. E.; Murray, D. L.; Thielen, K. R.; Williamson, E. E.; Eckel, L. J. Intracranial Gadolinium Deposition after Contrast-Enhanced MR Imaging. *Radiology* **2015**, *275*, 772–782.

14. Yang, H.; Zhang, C.; Shi, X.; Hu, H.; Du, X.; Fang, Y.; Ma, Y.; Wu, H.; Shi, X. Water-Soluble Superparamagnetic Manganese Ferrite Nanoparticles for Magnetic Resonance Imaging. *Biomaterials* **2010**, *31*, 3667–3673.

15. Ho, D.; Sun, X.; Sun, S. Monodisperse Magnetic Nanoparticles for Theranostic Applications. *Acc. Chem. Res*. **2011**, *44*, 875–882.

16. Lee, N.; Yoo, D.; Ling, D.; Cho, M.-H.; Hyeon, T.; Cheon, J. Iron Oxide Based Nanoparticles for Multimodal Imaging and Magnetoresponsive Therapy. *Chem. Rev.* **2015**, *115*, 10637–10689.

17. Ni, D.; Bu, W.; Ehlerding, E. B.; Cai, W.; Shi, J. Engineering of Inorganic Nanoparticles as Magnetic Resonance Imaging Contrast Agents. *Chem. Soc. Rev.* **2017**, *46*, 7438–7468.

18. Della Rocca, J.; Lin, W. Nanoscale Metal–Organic Frameworks: Magnetic Resonance Imaging Contrast Agents and Beyond. *Eur. J. Inorg. Chem.* **2010**, *24*, 3725–3734.

19. Sowers, M. A.; McCombs, J. R.; Wang, Y.; Paletta, J. T.; Morton, S. W.; Dreaden, E. C.; Boska, M. D.; Ottaviani, M. F.; Hammond, P. T.; Rajca, A.; Johnson, J. A. Redox-Responsive Branched-Bottlebrush Polymers for *in vivo* MRI and Fluorescence Imaging. *Nat. Commun.* **2014**, *5*, 5460–5467.

20. Zhou, Z.; Bai, R.; Munasinghe, J.; Shen, Z.; Nie, L.; Chen, X. T1–T2 Dual-Modal Magnetic Resonance Imaging: From Molecular Basis to Contrast Agents. *ACS Nano* **2017**, *11(6)*, 5227−5232.

21. Zhou, Z.; Huang, D.; Bao, J.; Chen, Q.; Liu, G.; Chen, Z.; Chen, X.; Gao, J. A Synergistically Enhanced T1–T2 Dual-Modal Contrast Agent. *Adv. Mater.* **2012**, *24*, 6223–6228.

22. Shin, T.-H.; Choi, J.-S.; Yun, S.; Kim, S.; Song, H.-T.; Kim, Y.; In Park, K.; Cheon, J. T1 and T2 Dual-Mode MRI Contrast Agent for Enhancing Accuracy by Engineered Nanomaterials. *ACS Nano* **2014**, *8(4)*, 3393–3401.

23. Zhang, L.; Liang, S.; Liu, R.; Yuan, T.; Zhang, S.; Xu, Z.; Xu, H. Facile Preparation of Multifunctional Uniform Magnetic Microspheres for T1-T2 Dual Modal Magnetic Resonance and Optical Imaging. *Colloids Surf. B Biointerfaces* **2016**, *144*, 344–354.

24. Choi, J. S.; Lee, J. H.; Shin, T. H.; Song, H. T.; Kim, E. Y.; Cheon, J. Self-Confirming "AND" Logic Nanoparticles for Fault-Free MRI. *J. Am. Chem. Soc.* **2010**, *132*, 11015−11017.

25. Im, G. H.; Kim, S. M.; Lee, D.-G.; Lee, W. J.; Lee, J. H.; Lee, I. S. Fe_3O_4/MnO Hybrid Nanocrystals as a Dual Contrast Agent for Both T1- and T2- Weighted Liver MRI. *Biomaterials* **2013**, *34*, 2069−2076.

26. Li, F.; Zhi, D.; Luo, Y.; Zhang, J.; Nan, X.; Zhang, Y.; Zhou, W.; Qiu, B.; Wen, L.; Liang, G. Core/Shell Fe_3O_4/Gd_2O_3 Nanocubes as T1–T2 Dual Modal MRI Contrast Agents. *Nanoscale* **2016**, *8*, 12826−12833.

27. Huang, G.; Li, H.; Chen, J.; Zhao, Z.; Yang, L.; Chi, X.; Chen, Z.; Wang, X.; Gao, J. Tunable T1 and T2 Contrast Abilities of Manganese-Engineered Iron Oxide Nanoparticles Through Size Control. *Nanoscale* **2014**, *6*, 10404−10412.

28. Wang, X.; Zhou, Z.; Wang, Z.; Xue, Y.; Zeng, Y.; Gao, J.; Zhu, L.; Zhang, X.; Liu, G.; Chen, X. Gadolinium Embedded Iron Oxide Nanoclusters as T1-T2 Dual-Modal MRI-Visible Vectors for Safe and Efficient siRNA Delivery. *Nanoscale* **2013**, *5*, 8098−8104.

29. Yang, L.; Zhou, Z.; Liu, H.; Wu, C.; Zhang, H.; Huang, G.; Ai, H.; Gao, J. Europium-Engineered Iron Oxide Nanocubes with High T1 and T2 Contrast Abilities for MRI in Living Subjects. *Nanoscale* **2015**, *7*, 6843−6850.

30. Wang, L.; Huang, J.; Chen, H.; Wu, H.; Xu, Y.; Li, Y.; Yi, H.; Wang, Y. A.; Yang, L.; Mao, H. Exerting Enhanced Permeability and Retention Effect Driven Delivery by Ultrafine Iron Oxide Nanoparticles with T1-T2 Switchable Magnetic Resonance Imaging Contrast. *ACS Nano* **2017**, *11*, 4582−4592.

31. Niu, D.; Luo, X.; Li, Y.; Liu, X.; Wang, X.; Shi, J. Manganese-Loaded Dual-Mesoporous Silica Spheres for Efficient T1- and T2-Weighted Dual Mode Magnetic Resonance Imaging. *ACS Appl. Mater. Interfaces* **2013**, *5*, 9942−9948.

32. Courant, T.; Roullin, V. G.; Cadiou, C.; Callewaert, M.; Andry, M. C.; Portefaix, C.; Hoeffel, C.; de Goltstein, M. C.; Port, M.; Laurent, S.; Elst, L. V.; Muller, R.; Molinari, M.; Chuburu, F. Hydrogels Incorporating GdDOTA: Towards Highly Efficient Dual T1/T2 MRI Contrast Agents. *Angew. Chem., Int. Ed.* **2012**, *51*, 9119− 9122.

33. Chen, Y.; Ai, K.; Liu, J.; Ren, X.; Jiang, C.; Lu, L. Polydopamine-Based Coordination Nanocomplex for T1/T2 Dual Mode Magnetic Resonance Imaging-Guided Chemo-Photothermal Synergistic Therapy. *Biomaterials* **2016**, *77*, 198−206.

34. Wang, L.; Lin, H.; Ma, L.; Jin, J.; Shen, T.; Wei, R.; Wang, X.; Ai, H.; Chen, Z.; Gao, J. Albumin-Based Nanoparticles Loaded with Hydrophobic Gadolinium Chelates as T1–T2 Dual-Mode Contrast Agents for Accurate Liver Tumor Imaging. *Nanoscale* **2017**, *9*, 4516−4523.

35. Borges, M.; Yu, S.; Laromaine, A.; Roig, A.; Suarez-Garcia, S.; Lorenzo, J.; Ruiz-Molina, D.; Novio, F. Dual T1/T2 MRI Contrast Agent Based on Hybrid SPION@Coordination Polymer Nanoparticles. *RSC Adv.* **2015**, *5*, 86779−86783.

36. Wang, G. D.; Chen, H.; Tang, W.; Lee, D.; Xie, J. Gd and Eu Co-Doped Nanoscale Metal–Organic Framework as a T1–T2 Dual-Modal Contrast Agent for Magnetic Resonance Imaging. *Tomography* **2016**, *2*, 179−187.

37. Zhu, W.; Liu, Y.; Yang, Z.; Zhang, L.; Xiao, L.; Liu, P.; Wang, J.; Yi, C.; Xu, Z.; Ren, J. Albumin/Sulfonamide Stabilized Iron Porphyrin Metal Organic Framework Nanocomposites: Targeting Tumor Hypoxia by Carbonic Anhydrase IX Inhibition and T1–T2 Dual Mode MRI Guided Photodynamic/Photothermal therapy. *J. Mater. Chem. B* **2018**, *6*, 265−276.

38. Guldris, N.; Argibay, B.; Kolen'ko, Y. V.; Carbó-Argibay, E.; Sobrino, T.; Campos, F.; Salonen, L. M.; Bañobre-López, M.; Castillo, J.; Rivas, J. Influence of the Separation Procedure on the Properties of Magnetic Nanoparticles: Gaining in vitro Stability and T1–T2 Magnetic Resonance Imaging Performance. *J. Colloid Interface Sci.* **2016**, *472*, 229−236.39. Adarsh, N. N.; Novio, F.; Ruiz-Molina, D. Coordination Polymers Built from 1,4-bis(imidazol-1-ylmethyl)benzene: from Crystalline to Amorphous. *Dalton Trans.* **2016**, *45*, 11233−11255.

40. Novio, F.; Lorenzo, J.; Nador, F.; Wnuk, K.; Ruiz-Molina, D. Carboxyl Group (-CO2H) Functionalized Coordination Polymer Nanoparticles as Efficient Platforms for Drug Delivery. *Chem. Eur. J.* **2014**, *20*, 15443−15450.

41.Aires, A.; Ocampo, S. M.; Cabrera, D.; de la Cueva, L.; Salas, G.; Teran, F. J.; Cortajarena, A. L. BSA-Coated Magnetic Nanoparticles for Improved Therapeutic Properties. *Mater. Chem. B* **2015**, *3*, 6239−6247.

42. Mariam, J.; Sivakami, S.; Dongre, P. M. Albumin Corona on Nanoparticles - a Strategic Approach in Drug Delivery. *Drug Delivery* **2016**, *23:8*, 2668−2676.

43. Nador, F.; Novio, F.; Ruiz-Molina, D. Coordination Polymer Particles with Ligand-Centred pH-Responses and Spin Transition. *Chem. Commun.* **2014**, *50*, 14570−14572.

44. Amorín-Ferré, L.; Busqué, F.; Bourdelande, J. L.; Ruiz-Molina, D.; Hernando, J.; Novio, F. Encapsulation and Release Mechanisms in Coordination Polymer Nanoparticles. *Chem. Eur. J.* **2013**, *19*, 17508–17516.

45. Xu, Z. Mechanics of Metal-Catecholate Complexes: The Roles of Coordination State and Metal Types. *Sci. Rep.* **2013**, *3*, 2914.

46. Avdeef, A.; Sofen, R. S.; Bregante, T. L.; Raymond K. N. Coordination Chemistry of Microbial Iron Transport Compounds. 9.1 Stability Constants for Catechol Models of Enterobactin. *J. Am. Chem. Soc*. **1978**, *100 (17)*, 5362–5370.

47. Li, Y.; Wen, J.; Qin, M.; Cao, Y.; Ma, H.; Wang, W. Single-Molecule Mechanics of Catechol-Iron Coordination Bonds. *ACS Biomater. Sci. Eng*. **2017**, *3 (6)*, 979–989.

48. Birben, E.; Murat Sahiner, U.; Sackesen, C.; Erzurum, S.; Kalayci, O. Oxidative Stress and Antioxidant Defense. *World Allergy Organ J.* **2012**, *5(1)*, 9–19.

49. Stohs, S. J.; Bagchi, D. Oxidative Mechanisms in the Toxicity of Metal Ions. *Free Radic. Biol Med.* **1995**, *18 (2)*, 321–336.

50. Fu, P. P.; Xia, Q.; Hwang, H.-M.; Ray, P. C.; Yu, H. Mechanisms of Nanotoxicity: Generation of Reactive Oxygen Species. *J. Food Drug Anal.* **2014**, *22*, 64–75.

51. Cotton, F. A.; Wilkinson, G.; Murillo, C. A.; Bochmann, M. in Advanced Inorganic Chemistry. *John-Wiley and Sons, Inc.* New York, 6th edn., **1999**, p. 761.

52. Chen, J. Y.; Tsao, G. C.; Zhao, Q.; Zheng, W. Differential Cytotoxicity of Mn(II) and Mn(III): Special Reference to Mitochondrial [Fe-S] Containing Enzymes. *Toxicol Appl Pharmacol.* **2001**, *175*, 160–168.

53. Wartenberg, N.; Fries, P.; Raccurt, O.; Guillermo, A.; Imbert, D.; Mazzanti, M. A Gadolinium Complex Confined in Silica Nanoparticles as a Highly Efficient T1/T2 MRI Contrast Agent. *Chem. Eur. J.* **2013**, *19*, 6980–6983.

54. Zhou, Z.; Tian, R.; Wang, Z.; Yang, Z.; Liu, Y.; Liu, G.; Wang, R.; Gao, J.; Song, J.; Nie, L.; Chen, X. Artificial Local Magnetic Field Inhomogeneity Enhances T_2 Relaxivity. *Nat. Commun.* **2017**, *8*, 15468.

55. Srivastava, S.; Awasthi, R.; Tripathi, D.; Rai, M. K.; Agarwal, V.; Agrawal, V.; Gajbhiye, N. S.; Gupta, R. K.; Magnetic-Nanoparticle-Doped Carbogenic Nanocomposite: An Effective Magnetic Resonance/Fluorescence Multimodal Imaging Probe. *Small* **2012**, *8*, 1099–1109.

56. Guo, J.; Ping, Y.; Ejima, H.; Alt, K.; Meissner, M.; Richardson, J. J.; Yan, Y.; Peter, K.; von Elverfeldt, D.; Hagemeyer, C. E.; Caruso, F. Engineering Multifunctional Capsules through the Assembly of Metal–Phenolic Networks. *Angew. Chem. Int. Ed.* **2014**, *53*, 5546–5551.

57. Wang, J.; de Keizer, A.; van Leeuwen, H. P.; Yan, Y.; Vergeldt, F.; van As, H.; Bomans, P. H. H.; Sommerdijk, N. A. J. M.; Stuart, M. A. C.; van der Gucht, J. Effect of pH on Complex Coacervate Core Micelles from Fe(III)-Based Coordination Polymer. *Langmuir*, **2011**, *27*, 14776–14782.

58. Rodríguez, E.; Simoes, R. V.; Roig, A.; Molins, E.; Nedelko, N.; Slawska-Waniewska, A.; Aime, S.; Arus, C.; Cabañas, M. E.; Sanfeliu, C.; Cerdán, S.; García-Martín, M. L. An Iron-

Based T1 Contrast Agent Made of Iron-Phosphate Complexes: In Vitro and in Vivo Studies. *Magn. Reson. Mater. Phys., Biol. Med*. **2007**, *20*, 27–37.

59. Schwert, D. D.; Richardson, N.; Ji, G.; Radüchel, B.; Ebert, W.; Heffner, P. E.; Keck, R.; Davies, J. A. Synthesis of Two 3,5-Disubstituted Sulfonamide Catechol Ligands and Evaluation of Their Iron(III) Complexes for Use as MRI Contrast Agents. *J. Med. Chem*. **2005**, *48*, 7482–7485.

60. Horcajada, P.; Chalati, T.; Serre, C.; Gillet, B.; Sebrie, C.; Baati, T.; Eubank, J. F.; Heurtaux, D.; Clayette, P.; Kreuz, C.; Chang, J.-S.; Hwang, Y. K.; Marsaud, V.; Bories, P.–N.; Cynober, L.; Gil, S.; Férey, G.; Couvreur, P.; Gref, R. Porous Metal–Organic-Framework Nanoscale Carriers as a Potential Platform for Drug Delivery and Imaging. *Nat. Mat*. **2010**, 9, 172–178.

61. Bouchard, L.-S.; Anwar, M. S.; Liu, G. L.; Hann, B.; Gray, J. W.; Wang, X.; Pines, A.; Chen, F. F. Picomolar Sensitivity MRI and Photoacoustic Imaging of Cobalt Nanoparticles. *Proc Natl Acad Sci* USA **2009**, *106*, 4085–4089.

62. Candiota, A. P.; Acosta, M.; Simoes, R. V.; Delgado-Goni, T.; Lope-Piedrafita, S.; Irure Yoldi, A.; Marradi, M.; Bomatí-Miguel, O.; Miguel-Sancho, N.; Abasolo, I.; Schwartz, Jr. S.; Santamaria, J.; Penadés, S.; Arús, C. A New ex Vivo Method to Evaluate the Performance of Candidate MRI Contrast Agents: a Proof-of-Concept Study. *J. Nanobiotechnology* **2014**, *12(12),* 1–14.

63. Mustafi, D.; Peng, B.; Foxley, S.; Makinen, M. W.; Karcmar, G. S; Zamora, M.; Ejnik, J.; Martin, H. New Vanadium-Based Magnetic Resonance Imaging Probes: Clinical Potential for Early Detection of Cancer. *J. Biol. Inorg. Chem.* **2009**, *14*, 1187–1197.

64. Marradi, M.; Alcántara, D.; de la Fuente, J.; García-Martín, M.; Cerdan, S.; Penadés, S. Paramagnetic Gd-Based Gold Glyconanoparticles as Probes for MRI: Tuning Relaxivities with Sugars. *Chem Commun.* **2006**, *26*, 3922–3924.

65. Gheorghe, D. E.; Cui, L.; Karmonik, C.; Brazdeikis, A.; Penaloza, J. M.; Young, J. K.; Drezek, R. A.; Bikram, M. Gold-Silver Alloy Nanoshells: a New Candidate for Nanotherapeutics and Diagnostics. *Nanoscale Res Lett*. **2011**, *6:554*, 1–12.

66. Saldana-Ruiz, S.; Soler-Martin, C.; Llorens, J. Role of CYP2E1-Mediated Metabolism in the Acute and Vestibular Toxicities of Nineteen Nitriles in the Mouse. *Toxicol Lett*. **2012**, *208(2)*, 125–132.

67. LASA; NC3Rs, Guidance on dose level selection for regulatory general toxicology studies for pharmaceuticals. Laboratory Animal Science Association & National Centre for the Replacement, R. a. R. o. A. i. R., Ed. London, **2009**.

68. Funk, F.; Ryle, P.; Canclini, C.; Neiser, S.; Geisser, P. The New Generation of Intravenous Iron: Chemistry, Pharmacology, and Toxicology of Ferric Carboxymaltose. *Arzneimittel-Forschung* **2010**, *60(6a)*, 345–353.

69. Cheng, W.; Ping, Y.; Zhang, Y.; Chuang, K. H.; Liu, Y. Magnetic Resonance Imaging (MRI) Contrast Agents for Tumor Diagnosis. *J. Healthc. Eng.* **2013**, *4(1)*, 23–45.

70. Gu, L.; Fang, R. H.; Sailor M. J.; Park, J. H. In Vivo Clearance and Toxicity of Monodisperse Iron Oxide Nanocrystals. *ACS Nano* **2012**, *6(6)*, 4947–4954.

71. Wei, Y.; Zhao, M.; Yang, F.; Mao, Y.; Xie, H.; Zhou, Q. Iron Overload by Superparamagnetic Iron Oxide Nanoparticles is a High Risk Factor in Cirrhosis by a Systems Toxicology Assessment. *Sci Rep*. **2016**, *6*, 29110.

72. Ramalho, J.; Ramalho, M.; Jay, M.; Burke, L. M.; Semelka, R. C. Gadolinium Toxicity and Treatment. *Magn. Reson. Imaging* **2016**, *34(10)*, 1394–1398.

73. Nador, F.; Wnuk, K.; García-Pardo, J.; Lorenzo, J.; Solorzano, R.; Ruiz-Molina, D.; Novio, F. Dual-Fluorescent Nanoscale Coordination Polymers via a Mixed-Ligand Synthetic Strategy and Their Use for Multichannel Imaging. *ChemNanoMat* **2018**, *4*, 183–193.

74. Adarsh, N. N.; Frias, C.; Ponnoth Lohidakshan, T.M.; Lorenzo, J.; Novio, F.; Garcia-Pardo, J.; Ruiz-Molina, D. Pt(IV)-Based Nanoscale Coordination Polymers: Antitumor Activity, Cellular Uptake and Interactions with Nuclear DNA. *Chem. Eng. J.* **2018**, *340*, 94–102.

75. Choi, H. S.; Liu, W.; Misra, P.; Tanaka, E.; Zimmer, J. P.; Ipe, B. I.; Bawendi, M. G.; Frangioni, J. V. Renal Clearance of Quantum Dots. *Nat Biotechnol.* **2007**, *25*, 1165–1170.

76. Crayton, S. H.; Elias, A.; Al-Zaki, A.; Cheng, Z.; Tsourkas, A. ICP-MS Analysis of Lanthanide-Doped Nanoparticles as a non-Radiative, Multiplex Approach to Quantify Biodistribution and Blood Clearance. *Biomaterials* **2012**, *33*, 1509–1519.

77. Yoo, J. W.; Chambers, E.; Mitragotri, S. Factors that Control the Circulation Time of Nanoparticles in Blood: Challenges, Solutions and Future Prospects. *Curr. Pharm. Des.* **2010**, *16*, 2298–2307.

Table of Contents